CHEMICAL PHYSICS

Probing vacancy behavior across complex oxide heterointerfaces
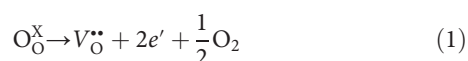
Jiaxin Zhu[1], Jung-Woo Lee[2], Hyungwoo Lee[2], Lin Xie[3], Xiaoqing Pan[3], Roger A. De Souza[4], Chang-Beom Eom[2], Stephen S. Nonnenmann[1]*

Oxygen vacancies ($V_O^{\bullet\bullet}$) play a critical role as defects in complex oxides in establishing functionality in systems including memristors, all-oxide electronics, and electrochemical cells that comprise metal-insulator-metal or complex oxide heterostructure configurations. Improving oxide-oxide interfaces necessitates a direct, spatial understanding of vacancy distributions that define electrochemically active regions. We show vacancies deplete over micrometer-level distances in Nb-doped SrTiO$_3$ (Nb:SrTiO$_3$) substrates due to deposition and post-annealing processes. We convert the surface potential across a strontium titanate/yttria-stabilized zirconia (STO/YSZ) heterostructured film to spatial (<100 nm) vacancy profiles within STO using ($T = 500°C$) in situ scanning probes and semiconductor analysis. Oxygen scavenging occurring during pulsed laser deposition reduces Nb:STO substantially, which partially reoxidizes in an oxygen-rich environment upon cooling. These results (i) introduce the means to spatially resolve quantitative vacancy distributions across oxide films and (ii) indicate the mechanisms by which oxide thin films enhance and then deplete vacancies within the underlying substrate.

INTRODUCTION

Complex oxide heterostructures generate tremendous research interest due to the unique electrical (*1*, *2*), ferroelectric (*3*, *4*), multiferroic (*5*), magnetic (*6*), and electrochemical phenomena (*7*, *8*) they exhibit. These breakthroughs resulted from advancements in the deposition and fabrication of oxide heterostructured films with atomic-level precision (*3*, *9*). Many functional complex oxide heterostructures partially comprise strontium titanate [SrTiO$_3$ (STO)] layers, the archetype perovskite system with a well-studied defect chemistry and multifunctional character (*10*). Two-dimensional electron gas (2DEG) formation at the LaAlO$_3$ (LAO)/STO interface (*1*) and colossal ionic conductivity at the YSZ/STO heterointerface (*11*) represent two examples of STO-based oxide pairs that exhibit unusual, yet tailorable, material properties using the highly sensitive interrelationship between structure (strain) and charge. While the origin of interfacial phenomena such as the formation of 2DEG or enhanced electrochemical activity has been attributed to electronic reconstruction (*1*, *12*), cation interdiffusion (*13*), or interfacial strain (*11*), other proposed mechanisms attribute the observed behavior to unique oxygen vacancy distributions in the substrate STO near heterointerfaces (*14*–*19*).

An oxygen vacancy is an intrinsic donor dopant in many transition metal oxides similar to STO, where the formation of the oxygen vacancy will be introduced either by acceptor doping (inadvertently or on purpose) or by the reduction reaction

$$O_O^X \rightarrow V_O^{\bullet\bullet} + 2e' + \frac{1}{2}O_2 \tag{1}$$

where two free electrons are donated to the conduction band through the creation of one oxygen vacancy. Pulsed laser deposition (PLD) has been shown to heavily reduce the underlying oxide substrate during thin-film fabrication, thus increasing the local oxygen vacancy concentration extending from the film-substrate interface (*18*–*21*). Although the mechanism is still obscure, an emerging body of work attributes this highly reduced state to metal oxide films scavenging oxygen from the underlying substrate and adjacent films even under nonreducing deposition atmosphere (*15*, *19*, *22*, *23*).

Studies using Hall effect measurements (*21*), Shubnikov–de Haas oscillations (*16*), and cathode luminescence (*17*) yielded evidence of the interfacial oxygen vacancy doping within the underlying STO substrate but did not spatially resolve quantitative oxygen vacancy distributions across the thickness direction of the heterostructured oxide interface. Aberration-corrected scanning transmission electron microscopy (STEM) (*24*) and electron energy loss spectroscopy (EELS) (*25*) studies both quantitatively resolve the oxygen vacancy concentration in perovskite (ABO$_3$) oxides with subnanometer resolution but typically limit the scan area to less than 10 nm; thus, information extending far (micrometers) from the interface has yet to be revealed. Conductive atomic force microscopy (c-AFM) was previously used to map the charge carrier density within LAO/STO cross sections with nanometer resolution (*14*), but required a cumbersome comparison between a uniformly doped Nb:STO reference sample and the heterostructure interfacial region with highly inhomogeneous vacancy concentrations. Moreover, determining whether transport depends on oxygen vacancies, rather than on other intrinsic defects such as strontium vacancies, requires using variable temperature studies.

A complete understanding of interfacial phenomenon in complex oxide heterostructures, especially those involving oxygen vacancy dynamics, requires in situ measurement techniques capable of resolving properties with nanometer resolution while operating within the standard solid oxide electroactive operation regime, which typically comprises elevated temperatures ($T > 500°C$) and ambient oxygen partial pressures. Commonly used characterization techniques for solid oxide devices, such as ambient-pressure x-ray photoelectron spectroscopy (AP-XPS) (*26*) and electrochemical impedance spectroscopy (EIS), operate under sub-ambient to ambient pressures (100 torr of atmosphere) and elevated temperatures. AP-XPS also has coarse (~10 μm) spatial resolution due to the beam spot size, while EIS does

[1]Department of Mechanical and Industrial Engineering, University of Massachusetts-Amherst, Amherst, MA 01003, USA. [2]Department of Materials Science and Engineering, University of Wisconsin-Madison, Madison, WI 53706, USA. [3]Department of Chemical Engineering and Materials Science, University of California, Irvine, Irvine, CA 92697, USA. [4]Institute of Physical Chemistry, RWTH Aachen University, Aachen 52056, Germany.
*Corresponding author. Email: ssn@umass.edu

not have any spatial resolution. Scanning surface potential microscopy (SSPM) is a modified two-pass local probe technique used to determine the surface potential of material surfaces with nanoscale precision (27), thus yielding highly localized physical and electrochemical properties. High temperatures present significant hurdles for local probe studies of energy-related material systems, where in situ SSPM under operating conditions, or so-called operando measurements, has only been recently introduced (28, 29). We previously used SSPM to characterize interfacial potential perturbations, active zone widths, and triple-phase boundary widths of solid oxide fuel cell electrode/electrolyte assemblies and CeO_2-based solid oxide electrolysis cell electrodes at intermediate operation temperatures ($T = 500°$ to $600°C$) with a customized miniature environmental chamber (30–33).

In this study, we measure local surface potential variations orthogonal to the interfaces of STO/YSZ multilayer oxide cross-sectional films using high-temperature SSPM. Here, the multilayer constituent oxide choices form a robust test structure enabling in situ visualization of vacancy distributions under both applied thermal and electrical stimuli. STO represents a model perovskite system with a well-studied defect chemistry and vacancy transport properties (34), while YSZ is a commonly used ionic conducting solid electrolyte with known oxygen scavenging behavior (15). We show surface potential variations across the interfacial regions, collected as a function of temperature and electrical bias. The results validate the existence of unique oxygen vacancy distributions that manifest as large, micrometer-level depletion regions induced under commonly applied PLD deposition environmental conditions, with implications for substrate selection.

RESULTS

In situ surface potential evolution across STO/YSZ multilayer films

Figure 1A shows an illustration of the high-temperature in situ potential scanning system for a 500-nm STO/500-nm YSZ/500-nm STO/ 500-nm YSZ multilayer film grown on the (001)-oriented 0.05 weight % (wt %) Nb:STO single crystal substrate. Here, a 100-nm aluminum film with a 25-nm platinum cap forms an Ohmic contact with Nb: STO, and a 25-nm platinum film serves as the top electrode. The low-magnification high-angle annular dark-field (HAADF) STEM image in Fig. 1B shows the deposited STO/YSZ multilayer film. From the high-magnification HAADF images and selected-area electron diffraction patterns of each layer, as shown in Fig. 1 (C and D), the first STO layer appears to have grown epitaxially on the Nb:STO substrate, while the first YSZ, second STO, and second YSZ layers all exhibit a columnar polycrystalline microstructure. Additional structural analysis by x-ray diffraction (XRD) is shown in fig. S1.

To effectively minimize any potential effects of lateral diffusion (Fig. 1A; y axis) to the measurement results, the sample was first cut in half lengthwise and then cut again and polished to create a quartered section of the original deposited structure, which enabled access to the center portion of the deposited film (fig. S2). Figure 2 shows the cross-sectional topographic and surface potential images (Fig. 2A) of the multilayer region collected in situ at a sample temperature of 500°C, respectively. Here, the stark contrast shift on the right-most portion of the topographic images indicates the location of the multilayer film edge. The potential profile (Fig. 2B) extracted from the surface potential image exhibits a rather unusual perturbation
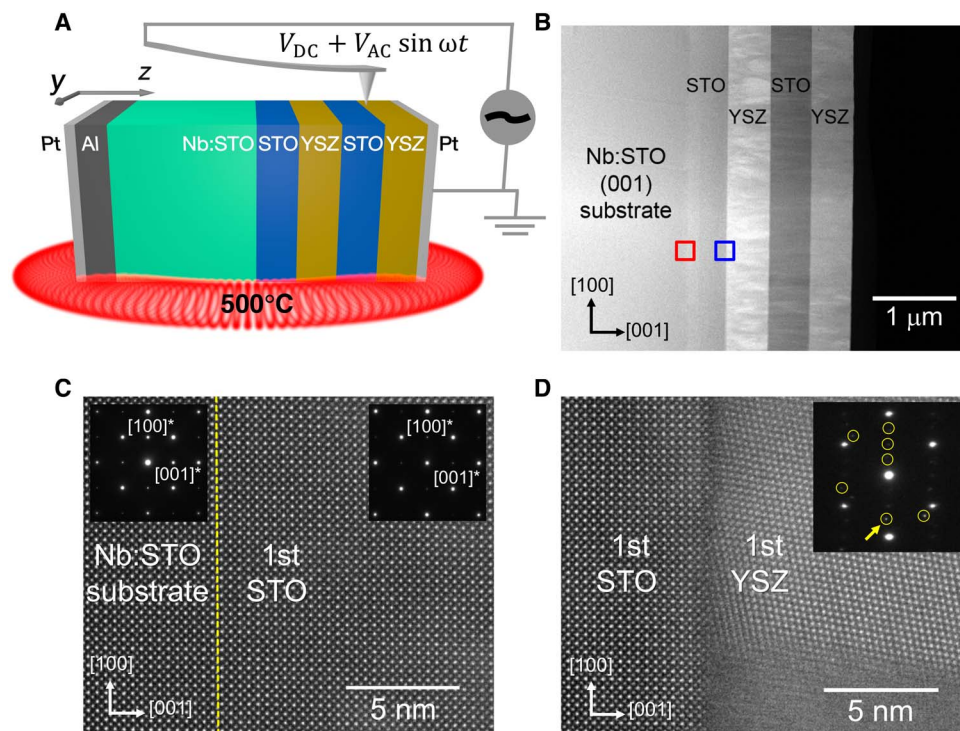
Fig. 1. The schematic of the measurement system and the structure of the multilayer oxide films. (**A**) Schematic of the high-temperature in situ potential scanning geometry. (**B**) Low-magnification HAADF image of the multilayer sample. (**C** and **D**) High-magnification HAADF images of interfaces between Nb:STO and first STO, first STO, and first YSZ layers, respectively. The insets show selected-area electron diffraction patterns of each layer. The yellow circles indicated by the arrow in (D) represent the polycrystallinity of the first YSZ layer. Images in (C) and (D) were collected from red and blue parts of (B), respectively.
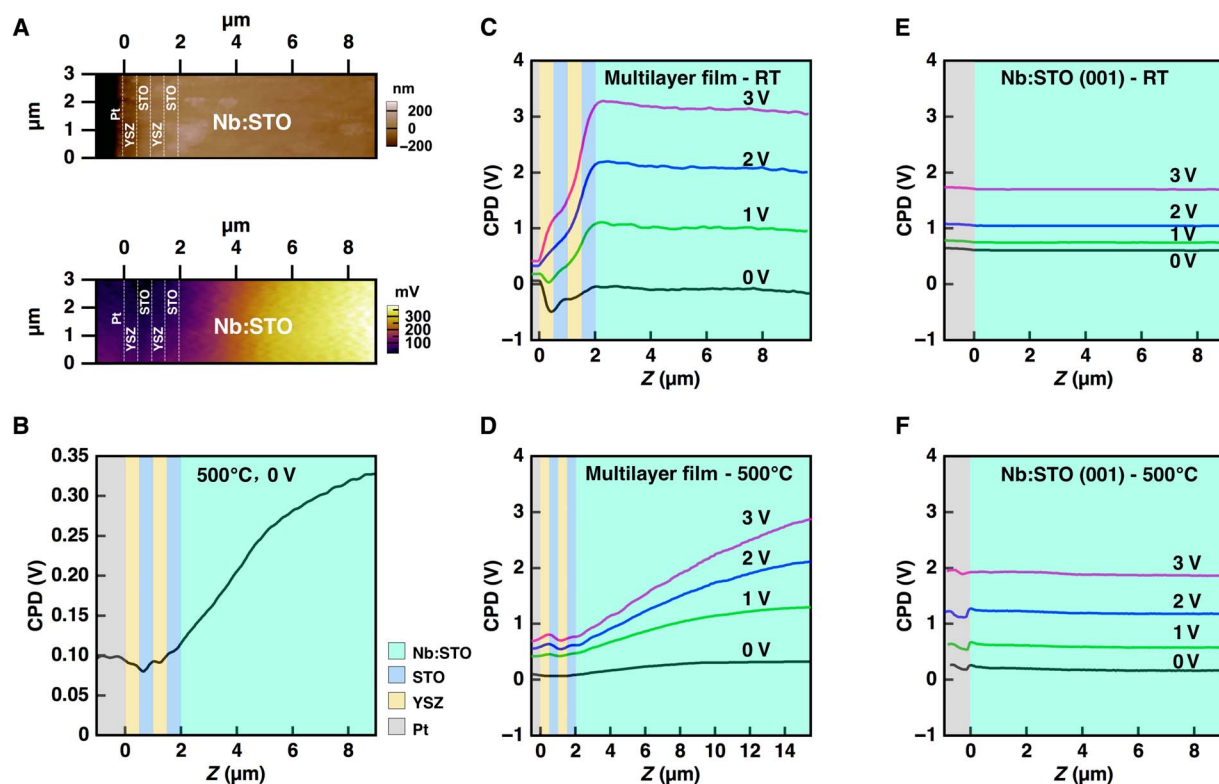
Fig. 2. A comparison of in situ surface potential on STO/YSZ multilayer oxide films and thermally treated Nb:STO(001) substrate under room and elevated (500°C) temperatures. (**A**) Topographic (top) and surface potential (bottom) images and (**B**) extracted potential profile results collected with biases of 0 V at 500°C. A large potential variation occurs across the Nb:STO substrate and continues throughout the multilayer film. (**C** and **D**) Potential profiles collected from STO/YSZ multilayer oxide films with biases ranging from 0 to 3 V at room temperature (RT) (C) and at 500°C (D) suggest electronic- and ionic-dominant transport, respectively. (**E** and **F**) Potential profiles collected on the thermally treated Nb:STO(001) substrate with biases ranging from 0 to 3 V at room temperature (E) and at 500°C (F) remain consistently flat across the sample.

near the Nb:STO/STO interface and extends approximately 7 μm at 0-V bias. As the oxidation-induced space-charge region typically spans tens of nanometers within Nb:STO (35), we contend that this drop must be induced by a different mechanism that occurs over a micrometer-level length scale.

Depletion regions and electronic-dominant versus ionic-dominant character

Nb:STO has two types of dopants: (i) intrinsic dopants, such as oxygen vacancies as donors and strontium vacancies as acceptors, and (ii) extrinsic dopants in the form of niobium donors (10). Considering the measurement temperature and applied bias, both Nb cations and Sr vacancies within STO are considered immobile in this study (36, 37). We can safely attribute, therefore, the surface potential variations occurring along the Nb:STO/STO interface to the diffusion and evolution of oxygen vacancy dopant concentrations.

Potential images were collected under various biases, at both elevated and room temperature, to decouple possible $Nb^{\bullet}_{Ti}$ and $V^{''}_{Sr}$ contributions to the surface potential perturbations observed in the Nb:STO/STO interfacial region. The potential profiles were extracted from the potential images by averaging over 20 lines parallel to the z axis, assuming that the potential along the y axis is constant. The potential profiles measured at room temperature (Fig. 2C) exhibit a potential drop that occurs predominantly within the STO/YSZ multilayer region, while the potential of the Nb:STO substrate remains

relatively constant. As the applied bias increased, the potential drop remained constrained to the 2-μm insulating multilayer region. The in situ SSPM measurements performed at 500°C required waiting 5 min to reach the steady-state current value after changing the bias. From Fig. 2D, the potential drop starts from the region in the Nb:STO substrate close to the STO film and extends further into the Nb:STO substrate as the applied bias increases. If these observed perturbations originated from variations in electronic conductivity, the trend would be observed at both room and elevated temperature. Because $Nb^{\bullet}_{Ti}$ and $V^{''}_{Sr}$ are immobile at 500°C, any potential drop induced by depletion of $Nb^{\bullet}_{Ti}$ or accumulation of $V^{''}_{Sr}$ would remain constant at 7 μm in depth under increased bias, which is not observed. Thus, we excluded any possible contributions from $Nb^{\bullet}_{Ti}$ and $V^{''}_{Sr}$ to this pronounced depletion-like region extending from the Nb:STO/STO interface.

The variations in the observed profiles are therefore due to the nature of the dominant charge carrier at these two temperatures. At room temperature, oxygen incorporation into the outer YSZ film does not occur, and thus, steady-state ionic currents under bias are negligible. Electronic current, although also low, becomes the dominant carrier transport mechanism across the multilayer films at room temperature. In this case, intrinsic STO and YSZ films are orders of magnitude less electronically conductive than Nb:STO, constraining the potential drop to the multilayer region. At 500°C, YSZ becomes an oxygen ion conductor with negligible electronic conductivity and,

hence, serves a role as an electron blocker in this electrochemical assembly. The Nb:STO substrate and STO films in this sample both have a relatively large oxygen vacancy concentration, as shown later, and thus are endowed with appreciable ionic conductivity (38). As a result, the ionic current becomes dominant at elevated temperatures and the potential variation under bias indicates ionic transport variation across the substrate and films. While in the bulk Nb:STO substrate ($Z < 6$ μm in Fig. 2D) the oxygen vacancy concentration is almost constant, the interfacial region adjacent to the multilayer films displays a depletion of oxygen vacancy concentration that significantly reduces its ionic conductivity and results in a surprisingly large potential drop in this region under bias. The trend of the potential drop extending deeper into the Nb:STO substrate with increasing bias is a steady-state response of the material according to the constant current measured during SSPM scanning (see the Supplementary Materials). Once external bias was removed, the contact potential difference (CPD) profile returned to its initial state after a 5- to 10-min relaxation until the current reached steady state.

To further validate the assumption of oxygen vacancy–dominated potential perturbations, we prepared a (001)-oriented 0.05 wt % Nb: STO control sample without the multilayer film under the identical (both temperature and gas atmosphere) thermal budget used during the PLD process to fabricate the STO/YSZ multilayer oxide films. Figure 2 (E and F) presents the SSPM results of the control sample collected at room temperature and at 500°C, respectively. Unlike the STO/YSZ multilayer oxide films, the potential profiles of the control sample collected at 500°C remain relatively flat and do not have an appreciable potential drop. Without the YSZ films present to serve as an electron blocker, the electronic conductivity again becomes the dominant mechanism at both room temperature and at 500°C under bias. As a result, the potential profiles of the thermally treated Nb: STO substrate display a consistent, flat trend at different measurement temperatures. Here, the only difference between the 500°C and room temperature profiles is the contrasting absolute potential values at various biases. The presence of a surface water meniscus during room temperature measurements likely causes the measured potential variation, as previously reported from other oxide surfaces (39). The primary reason that the profiles in Fig. 2 (E and F) differ from those in Fig. 2C is because there are no electronic insulating films on Nb: STO substrates. As bias is only applied to the substrate, the electrostatic potential will drop gradually across its entire thickness (1 mm) instead of only dropping in the 2-μm-thick multilayer film region as seen in Fig. 2C, so the drop appears to be "stretched" or flat over such a larger distance.

Local oxygen vacancy distributions within Nb:STO and STO regions

Clarifying the mechanism underlying the oxygen vacancy–induced potential perturbation and transport phenomena requires mapping and quantifying oxygen vacancy distributions across the multilayer heterostructured regions. Previous SSPM or Kelvin probe force microscopy (KPFM) studies successfully analyzed collected potential profiles to yield distributions of dopant concentrations within semiconductors (40, 41) and metal oxides (42, 43), including nonuniform doping distributions along silicon nanowires (40), quantified two-dimensional doping profiles within ZnO thin films (43), and quantitative determination of band alignment across depth of solar cell multilayers (41). Here, the oxygen vacancy concentration within STO is estimated in a similar manner by assuming that oxygen vacancies

exist as an n-type dopant and contribute two free carriers to the conduction band per vacancy.

A simple electronic energy model relates the surface potential profiles to the dopant concentration (43). Fundamentally, SSPM measures the CPD between the tip and the sample surface. Under zero applied bias, the CPD becomes the work function difference between the tip and the sample, that is

$$V_{CPD} = \frac{\phi_{tip} - \phi_{sample}}{q} = \frac{\phi_{tip} - [\chi + [E_C - E_F]]}{q} \quad (2)$$

where ϕ_{tip} and ϕ_{sample} represent the work functions of the tip and the sample, respectively; χ is the electron affinity of the oxide; E_C is the energy level of the conduction band; and E_F is the Fermi level.

Because the absolute tip work function is unknown, we used the 0.05 wt % Nb-doped STO substrate as the reference point. An estimate of the sample charge carrier density n is

$$n = N_C F_{1/2}(\eta) \quad (3)$$

where N_C is the effective density of states, $F_{1/2}$ is the Fermi-Dirac integral, and η is a function of $(E_F - E_C)$.

As measurements occurred at temperature of 500°C, it is reasonable to assume that all the oxygen vacancies are doubly ionized (38), i.e., $n = [Nb_{Ti}^{\bullet}] + 2[V_O^{\bullet\bullet}]$. The $[Nb_{Ti}^{\bullet}]$ value is calculated from the substrate doping amount (0.05 wt % Nb in STO). Combined with Eqs. 2 and 3, the variation in charge carrier density is therefore related to the variation of oxygen vacancy concentration as

$$[V_O^{\bullet\bullet}] = \frac{1}{2}\left[N_C F_{1/2}\left(\frac{qV_{CPD} + \chi - \phi_{tip}}{k_B T}\right) - [Nb_{Ti}^{\bullet}] \right] \quad (4)$$

Therefore, we used Eq. 4 to calculate the oxygen vacancy dopant concentration by substituting the local V_{CPD} values observed across the multilayer films via SSPM. The detailed computation processes are included in the Supplementary Materials. A schematic band diagram correspondent to the ~7-μm potential perturbation at the Nb: STO/STO interface is demonstrated in Fig. 3A. A similar approach was recently used to probe the oxygen vacancy dynamics in STO (44); however, the interpretation of the results reversed the relationship between work function and relative oxygen vacancy concentration. In that study, areas exhibiting a higher work function were considered to be $[V_O^{\bullet\bullet}]$ rich. However, as an n-type dopant, higher oxygen vacancy concentrations push the Fermi level toward the conduction band, which necessitates a reduction in the relative offset $E_C - E_F$ and subsequently a lower work function.

Figure 3B shows a plot of the surface potential and corresponding oxygen vacancy concentration profile as a function of position. This profile, collected orthogonal to the multilayered oxide film interface, displays a region heavily depleted of oxygen vacancies adjacent to the Nb:STO/STO interface. The Nb:STO bulk region appears strongly reduced based on the surface potential conversion ($[V_O^{\bullet\bullet}] \approx 3.1 \times 10^{20}$ cm^{-3}), much higher than the expected value for a 0.05 wt % (0.1 atomic %) Nb:STO substrate ($[V_O^{\bullet\bullet}] \leq 10^{15}$ cm^{-3}) (45). A separate 0.05 wt % Nb:STO substrate without film, prepared under the identical thermal budget used to create the STO/YSZ multilayer oxide
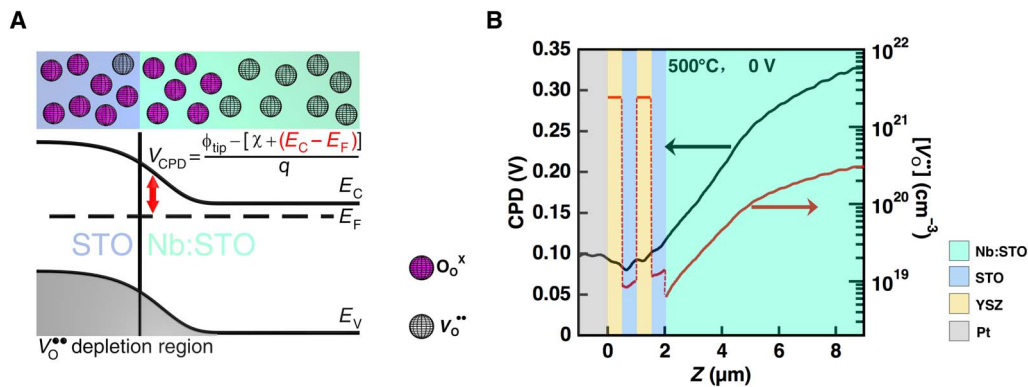
Fig. 3. The oxygen vacancy concentration distribution across STO/YSZ multilayer oxide films. (**A**) Illustrated schematic of the band diagram at the Nb:STO/STO interface. Here, the contact potential difference (CPD) measured by SSPM is used to determine the offset of the Fermi band from the conduction band, as a function of position in the z direction. (**B**) Surface potential profile collected in situ at 500°C (red) and resulting oxygen vacancy concentration distribution across the STO/YSZ multilayer oxide films (black). The oxygen vacancy concentration decreased from STO to YSZ near the interface and extends ~7 μm into the bulk Nb:STO substrate. The calculated oxygen vacancy concentration in YSZ films indicates an abrupt increase compared to the oxygen vacancy concentration in STO probed and derived from the surface potential (dashed red lines).

films, exhibited a surface potential profile nearly identical to that measured from the as-received Nb:STO substrate (fig. S3), indicating that only a negligible amount of $V_O^{\bullet\bullet}$ was created by thermal treatment alone. Therefore, the large amount of vacancies must be created during PLD film deposition. An unusual feature in the concentration profile shows that $[V_O^{\bullet\bullet}]$ decreased from ~3.1×10^{20} cm^{-3} in the bulk to 6.3×10^{18} cm^{-3} at the Nb:STO/STO-1 interface, lower than the dopant concentration of Nb (1.7×10^{19} cm^{-3}). The $[V_O^{\bullet\bullet}]$ value in the Nb:STO bulk derived from the SSPM profile strongly deviates from the expected value at equilibrium with the measurement conditions (ambient; $T = 500$°C). As PLD-induced reduction of the substrate should yield enhancements in vacancy concentration, this counterintuitive observance of the interfacial vacancy depletion region suggests that a secondary mechanism such as oxygen reincorporation must occur sequentially during sample preparation, which will be introduced in the next section.

In the multilayer region (Fig. 3B), the oxygen vacancy concentration gradient becomes relatively flat in the first STO film (adjacent to the Nb:STO substrate), decreasing from 1.4×10^{19} cm^{-3} to 1.2×10^{19} cm^{-3} across the film. In the second STO film (between YSZ layers), the oxygen vacancy concentration also displays a small negative gradient ranging from 1.0×10^{19} cm^{-3} to 8.9×10^{18} cm^{-3}. Unlike STO, oxygen vacancies are not considered a dopant within YSZ, yielding no direct way to correlate the oxygen vacancy concentration to the charge carrier density in YSZ. Instead, a positively charged defect compensates the negative charge induced by substituting Zr^{4+} with Y^{3+}. Here, we calculated the oxygen vacancy concentration in the YSZ regions directly from the yttrium substituent concentration [8 mole percent (mol %) Y_2O_3]. Additional oxygen vacancies may be present in the YSZ layers, generated either by reduction or from redistribution from the STO layers (46); their amount will, however, be relatively low as compared with the amount due to the yttrium substituent. The result is a significant difference (two orders of magnitude) in oxygen vacancy concentration in YSZ compared to the STO films. The STO/YSZ interface exhibited a slightly higher potential than the center of the first YSZ and second STO films, which is likely attributed to the accumulation of oxygen vacancies. The potential profile in the first YSZ layer followed a "V" shape, indicative of excess oxygen vacancies diffusing from the STO layer to the YSZ layer to reach electrochemical

potential equilibrium across the multilayer films (45). Assuming that the valley of the potential profile in YSZ is neutral, and by applying the parallel capacitor model, $\Delta V = \Delta\sigma \frac{d}{\varepsilon}$, the calculated excess oxygen vacancy concentration is on the order of 10^9 cm^{-3}, which is negligible compared to the large intrinsic oxygen vacancy concentration in the YSZ layer. In the second YSZ layer, the potential profile is nearly constant. Therefore, it is reasonable to assume a constant $[V_O^{\bullet\bullet}]$ across both YSZ layers with regard to the existence of a limited amount of $[V_O^{\bullet\bullet}]$ redistribution from STO to YSZ, as previous defect thermodynamic studies proposed (46).

Extreme reduction of Nb:STO substrates during PLD

The large amounts of oxygen vacancies and electrons in the Nb:STO substrate were likely generated during the deposition by PLD of the multilayer heterostructure, as suggested in other PLD film studies (18–21). The mechanism by which the substrate is reduced is illustrated in Fig. 4. During film deposition, we suppose that not all of the oxygen from the target is transferred to the film and that there is negligible incorporation of oxygen from the gas phase into the films. As a consequence, the growing film is severely oxygen deficient and scavenges oxygen, therefore, from the substrate and buried films (Fig. 4, A and B), a process previously verified by secondary ion mass spectrometry (SIMS) (19, 22) and in situ synchrotron-based x-ray techniques (23). Here, we can show that in our case the entire substrate was reduced by considering the reduction kinetics and the deposition time. Because reduction of the substrate involves the chemical diffusion of oxygen out of the substrate and into the film(s), i.e., the ambipolar diffusion of oxygen ions and electrons, the relevant kinetic parameter is the chemical diffusion coefficient of oxygen. For the deposition conditions, this quantity is given by (47) $D_O^\delta = 3D_V$ (with D_V being the diffusion coefficient of oxygen vacancies). With the literature value (48) of $D_V = 10^{-5.25}$ cm^2 s^{-1} at 750°C and the total deposition time (from the deposition of the first film until the end of the deposition of the final film) of $t_{dep} = 363$ min, one obtains a characteristic diffusion length (i.e., the spatial extent of reduction) of

$$\sqrt{D_O^\delta t_{dep}} = \sqrt{3D_V t_{dep}} \approx 6 \text{ mm}$$. This is many times larger than the substrate thickness (of 1 mm), thus confirming that the entire substrate was reduced during deposition. Further evidence is related to
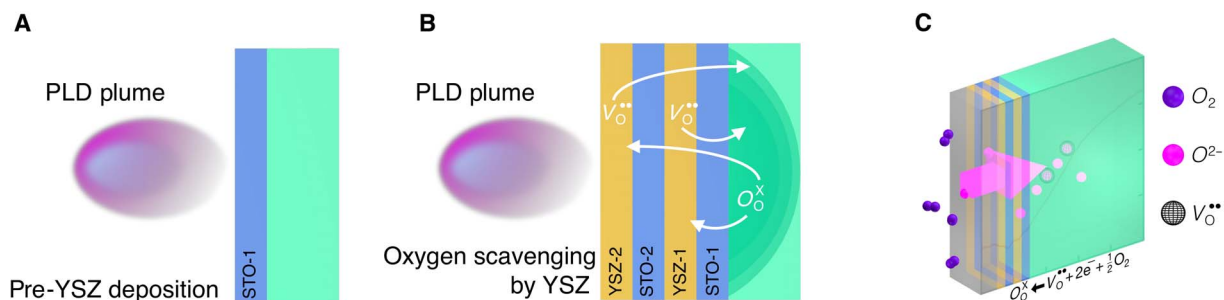
Fig. 4. The PLD induced substrate reduction and reoxidation process. (**A**) Deposited films scavenge oxygen from the substrate due to the limited oxygen exchange rate with the atmosphere in the PLD chamber. (**B**) Reduction of the substrate becomes more severe with the increasing thickness of the deposited films and the introduction of subsequent layers. (**C**) Mechanism of the formation of large oxygen vacancy annihilation region. After deposition, the oxygen incorporates back into the substrate through the multilayer films as the PLD chamber is backfilled with ~600 torr of oxygen and cooled from 750°C.

our four-layer deposited film being 2 μm in total thickness; this is much larger than the recently studied 150-nm $Sr_{0.98}La_{0.02}TiO_3$ (SLTO) thin film deposited under similar deposition condition on an STO substrate, and this thinner film already reduced the entire substrate (*18*).

We can calculate quantitatively not only the spatial extent of reduction but also the degree of reduction. Specifically, knowing n and $[V_O^{\bullet\bullet}]$ in the Nb:STO substrate (see previous section), one can calculate an effective oxygen partial pressure pO_2^{eff} in the highly reduced bulk of the substrate, i.e., the hypothetical oxygen partial pressure in the gas phase, if the substrate and surrounding gas phase were in equilibrium. Using literature data (*10*) for the equilibrium constant of reduction of STO, $K_{red}(T)$, we find this effective oxygen partial pressure to $pO_2^{eff} = (K_{red}(T)/(n^2[V_O^{\bullet\bullet}]))^2 \sim 10^{-41}$ bar. Hence, during the deposition, the substrate became increasingly reduced, reaching the level of $pO_2^{eff} \sim 10^{-41}$ bar at the end of the procedure. pO_2^{eff} in the films at the end of the procedure must have been at least slightly lower than this value (if not several orders of magnitude lower), because the chemical diffusion of oxygen takes place from regions of higher pO_2^{eff} (substrate) to regions of lower pO_2^{eff} (growing films). In this way, this result confirms that the growing films were not in equilibrium with the gas phase during deposition because the oxygen pressure in the PLD chamber ($>10^{-6}$ bar) was many orders of magnitude higher than this effective oxygen partial pressure.

Having considered in detail the movement of oxygen during film growth, we now turn to the movement of oxygen after film growth. Upon cooling the structure, a process initiated at 750°C, but in ~600 torr of O_2, a reoxidation front begins to penetrate into the films and then into the substrate. This reoxidation process requires (just like the reduction process) the chemical diffusion of oxygen (the ambipolar diffusion of oxygen ions and electronic species) through the various layers. In contrast to the reduction process, however, the reoxidation process also requires the chemical incorporation of oxygen at the exposed YSZ surface, i.e., molecular oxygen in the gas phase needs to be dissociated and reduced to oxygen ions, which are then incorporated into the YSZ solid. Penetrating into the structure, the incorporated oxygen fills some of the oxygen vacancies and annihilates some of the electrons. Because the sample is being cooled, and both diffusion kinetics and surface reaction kinetics are strongly thermally activated, the reoxidation front does not have enough time at a sufficiently high temperature to penetrate far into the substrate (fig. S5). This explains why the vacancy concentration is only diminished over ~7 μm into bulk Nb:STO. Here, it is important to note, first, that sufficient electronic species are present initially in all layers (STO and YSZ) due to the high

degree of reduction ($pO_2^{eff} \leq 10^{-41}$ bar), which permits chemical incorporation of oxygen at the YSZ surface (*49*) and chemical diffusion of oxygen through the layers. Second, incorporation and diffusion through the deposited films will occur only until there are insufficient electrons in the YSZ layers (YSZ, with its higher reduction enthalpy, will have a lower concentration of electronic charge carriers at given T and pO_2). As a consequence, the outermost YSZ layer prevents the underlying structure from attaining equilibrium with the external atmosphere, although it is a highly oxidizing environment. Comparatively, STO is less reactive than YSZ and is able to tolerate higher oxygen deficiency; thus, it is less likely to severely reduce the underlying substrate (fig. S6).

The next procedure to be regarded is annealing the multilayer film under ambient air (oxygen partial pressure of ~160 torr) at 600°C for 24 hours. Oxygen is now able to incorporate directly via the exposed cross-sectional surface instead of diffusing through the YSZ films and dramatically diminishes $[V_O^{\bullet\bullet}]$ in the bulk. As shown in Fig. 5, the absolute CPD value, under an applied bias of 0 V, is close to the as-received Nb:STO surface potential (fig. S3), which indicates that $Nb_{Ti}^{\bullet}$ serves as the dominant contributor to the charge carrier density, while the oxygen vacancy concentration has been suppressed orders of magnitude lower than $[Nb_{Ti}^{\bullet}]$, thus yielding a flat uniform profile across the entire substrate attributed to the uniform Nb dopant concentration. After annealing, the bias-dependent potential perturbation present in the as-deposited multilayer film (Fig. 2D) near the Nb:STO/STO interface disappeared as well. Because $[V_O^{\bullet\bullet}]$ has been vastly reduced, the ionic conductivity in the Nb:STO substrate and STO films at high temperature is negligible; as $Nb_{Ti}^{\bullet}$ becomes the dominant charge carrier contribution, the evolution of potential profiles measured at elevated temperature under bias now indicates electronic conductivity variation. With $[Nb_{Ti}^{\bullet}] = 1.7 \times 10^{19}$ cm^{-3}, the Nb:STO substrate is electrically conductive, while the STO and YSZ layers are relatively insulating. As a result, the potential profile throughout the Nb:STO substrate remains consistently flat under increasing bias despite the offset change due to the electrostatic potential applied, and the potential drop occurs primarily in the multi-layer region.

DISCUSSION

This study combines the ability to profile vacancy distributions with the systematic evaluation of heterostructured thin-film components to highlight the extent of PLD-induced defect levels in oxide substrates, which affects many interfacial phenomena. We produced a quantitative
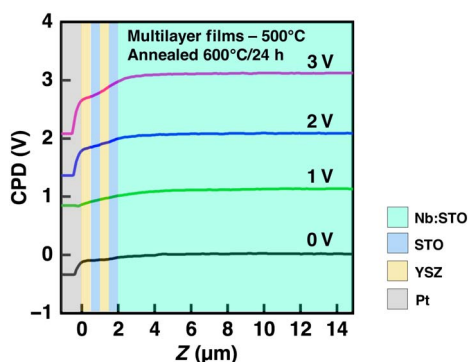
Fig. 5. The effects of annealing in oxidizing environments on the evolution of STO/YSZ multilayer surface potential profiles. The surface potential of the STO/YSZ multilayer films annealed at 600°C for 24 hours under ambient conditions, measured at 500°C in situ. The annealing process drastically reduces $[V_O^{\cdot\cdot}]$, and the potential profile becomes consistently flat across the Nb:STO substrate as compared to the as-prepared profiles of the same sample in Fig. 2D.

oxygen vacancy concentration profile derived directly from local surface potential perturbations measured from cross-sectional STO/YSZ multilayer oxide films in ambient atmosphere at high temperatures (500°C), in situ, with nanoscale resolution (<100 nm). The semiconductor dopant analysis used to convert surface potentials to vacancy distributions could be applied to other transition metal oxides in which oxygen vacancies are donor dopants. This process yields unprecedented, spatialized information of the fundamental building blocks driving functionality at the nanoscale, which affects systems ranging from resistive switching in perovskite-type oxides (50) to superconducting/ferromagnetic behavior at the interface of LAO/STO heterostructures (1, 2, 6). The evolution of the surface potential within the Nb-doped STO substrate with various STO and YSZ thin-film layers provided direct evidence of extreme reduction under commonly used PLD deposition conditions that result from the deposited layers scavenging oxygen from the substrate, thus yielding enhanced bulk oxygen vacancy concentrations. Cooling in oxygen likely oxidizes the deposited films considerably, yet leaves a portion of the substrate in a highly reduced state. For multilayer heterostructures, all layers may not have the same oxygen content or the same physical properties, depending on the nature of the materials making up the heterostructure and the cooling procedure. We note that other commonly used substrates, such as LAO, MgO, and various scandates, are less likely to be reduced (19) and could potentially be used to avoid these profiles in the defect evolution during the deposition process. The transition of large surface potential gradients found within the substrates supporting as-prepared PLD-deposited multilayer films to nominally flat profiles after a 600°C oxidizing anneal confirms the direct contributions of local vacancy concentrations on in situ potential perturbations. We thus expect that one general approach toward new functional heterostructured architectures could involve controlling oxygen reincorporation across scavenging/non-scavenging heterointerfaces using deliberate cooling parameters combined with the selection of more stable substrates to achieve tailorable interfacial vacancy concentrations within predefined layers. Last, the results presented here also promote the use of in situ scan probe techniques to investigate vacancy-mediated phenomena in complex oxide heterostructures under harsh environments, including electrochemical redox activity.

MATERIALS AND METHODS

STO/YSZ multilayers were grown on (001)-oriented 0.05 wt % Nb-doped STO (Nb:STO) single crystal substrates by PLD. Before deposition, Nb:STO substrates (1 mm thickness) were etched by a buffered hydrogen fluoride (HF) solution for 60 s and subsequently annealed at 1000°C in an oxygen atmosphere for 6 hours to achieve a TiO_2-terminated and atomically smooth surface. With the substrate adhered to the heater block with silver paste, the YSZ and STO layers were grown at 750°C in oxygen partial pressures of 1 and 10 mtorr for YSZ and STO, respectively. The YSZ target (8 mol %) was used for the YSZ film. Each layer was grown in sequence without breaking the vacuum, and the thickness of each layer was fixed at 500 nm by deposition of STO and YSZ layers for 68 and 86 min, respectively. The time to change a target and to prepare deposition of the next layer was ~20 min. After the deposition, the chamber was backfilled with ~600 torr of oxygen, and the oxygen pressure was kept during a cooldown. To effectively minimize any potential effects of lateral diffusion and obtain a smooth cross section, the sample was first cut in half lengthwise and then cut again and mechanically polished to create a quartered section of the original deposited structure. The sample size was ~2 mm × 2 mm (polished area) × 1 mm (thickness). Thereafter, Pt/Al (100 nm/25 nm) and Pt (25 nm) were deposited by radio frequency magnetron sputtering on the bottom of Nb:STO substrates and the top of YSZ films, respectively.

The crystal structure of the sample was analyzed by a high-resolution four-circle XRD machine with a Cu Kα (λ = 1.5406 Å) source (Bruker D8 Advance). HAADF STEM experiments were carried out on an FEI Titan 60-300 microscope equipped with double aberration correctors, and its resolution in STEM mode is ~0.6 Å. The accelerating voltage, convergence angle of the incident electrons, and collection angle for HAADF imaging are 300 kV, 25 mrad, and 79 to 200 mrad, respectively.

SSPM measurements were performed using a commercial AFM (Asylum Research MFP-3D, Santa Barbara, CA) outfitted with a customized miniature environmental chamber to produce a sample temperature of 500°C in ambient air (oxygen partial pressure of ~160 Torr). Conducting a calibration SSPM scan of the as-received 0.05 wt % Nb-doped STO reference sample cross-sectional surface enabled the collection of the CPD between the reference sample and the tip, which when averaged and added to the work function of 0.05 wt % Nb-doped STO yielded the work function of the pure platinum tips (RMN-25Pt400B; see the Supplementary Materials).

The cross-sectional measurement configuration required an initial tip placement close to the sample edge before scanning commenced. Subsequent adjustments to the x-axis offsets provided fine translation of the tip toward the multilayer oxide film interfaces, where sharp drops within the trace/retrace profiles confirmed that the tip reached the edge and measurements could begin. SSPM imaging subjected samples to sequentially applied lateral biases of 0, 1, 2, and 3 V orthogonal to the multilayer interfaces.

SUPPLEMENTARY MATERIALS

Supplementary material for this article is available at http://advances.sciencemag.org/cgi/content/full/5/2/eaau8467/DC1

Section S1. Out-of-plane XRD diffraction pattern of the multilayer films
Section S2. Sample geometry and preparation process after film deposition
Section S3. Steady-state currents of multilayer films during in situ SSPM at 500°C
Section S4. Oxygen vacancy concentration calculation
Section S5. Oxygen vacancy concentrations of reference samples
Section S6. Temperature profile during cooling process
Section S7. In situ SSPM on YSZ/Nb:STO and STO/Nb:STO control samples

Fig. S1. θ-2θ XRD pattern of STO/YSZ/STO/YSZ multilayer films on Nb:STO (001) substrate.
Fig. S2. Cut/polish sequence, possible oxygen incorporation pathways, and scan geometry.
Fig. S3. Current measured on multilayer films under 0 to 3 V at 500°C.
Fig. S4. SSPM calibration data collected on different STO substrates.
Fig. S5. The temperature versus time (cooling) curve of the sample upon chamber backfill.
Fig. S6. SSPM, Nb:STO/YSZ film (10 mtorr), Nb:STO/STO film, Nb:STO/YSZ film (1 mtorr).
References (51–54)

REFERENCES AND NOTES

1. A. Ohtomo, H. Y. Hwang, A high-mobility electron gas at the LaAlO3/SrTiO3 heterointerface. *Nature* **427**, 423–426 (2004).
2. N. Reyren, S. Thiel, A. D. Caviglia, L. F. Kourkoutis, G. Hammerl, C. Richter, C. W. Schneider, T. Kopp, A.-S. Rüetschi, D. Jaccard, M. Gabay, D. A. Muller, J.-M. Triscone, J. Mannhart, Superconducting interfaces between insulating oxides. *Science* **317**, 1196–1199 (2007).
3. C. H. Ahn, K. M. Rabe, J.-M. Triscone, Ferroelectricity at the nanoscale: Local polarization in oxide thin films and heterostructures. *Science* **303**, 488–491 (2004).
4. D. G. Schlom, L.-Q. Chen, C.-B. Eom, K. M. Rabe, S. K. Streiffer, J.-M. Triscone, Strain tuning of ferroelectric thin films. *Annu. Rev. Mater. Res.* **37**, 589–626 (2007).
5. R. Ramesh, N. A. Spaldin, Multiferroics: Progress and prospects in thin films. *Nat. Mater.* **6**, 21–29 (2007).
6. A. Brinkman, M. Huijben, M. van Zalk, J. Huijben, U. Zeitler, J. C. Maan, W. G. van der Wiel, G. Rijnders, D. H. Blank, H. Hilgenkamp, Magnetic effects at the interface between non-magnetic oxides. *Nat. Mater.* **6**, 493–496 (2007).
7. Y. Chen, Z. Cai, Y. Kuru, W. Ma, H. L. Tuller, B. Yildiz, Electronic activation of cathode superlattices at elevated temperatures - source of markedly accelerated oxygen reduction kinetics. *Adv. Energy Mater.* **3**, 1221–1229 (2013).
8. M. Sase, F. Hermes, K. Yashiro, K. Sato, J. Mizusaki, T. Kawada, N. Sakai, H. Yokokawa, Enhancement of oxygen surface exchange at the hetero-interface of (La,Sr)CoO₃ / (La,Sr)₂CoO₄ with PLD-Layered films. *J. Electrochem. Soc.* **155**, B793–B797 (2008).
9. P. Zubko, S. Gariglio, M. Gabay, P. Ghosez, J.-M. Triscone, Interface physics in complex oxide heterostructures. *Annu. Rev. Condens. Matter Phys.* **2**, 141–165 (2011).
10. R. Moos, K. H. Hardtl, Defect chemistry of donor-doped and undoped strontium titanate ceramics between 1000° and 1400° C. *J. Am. Ceram. Soc.* **80**, 2549–2562 (1997).
11. J. Garcia-Barriocanal, A. Rivera-Calzada, M. Varela, Z. Sefrioui, E. Iborra, C. Leon, S. J. Pennycook, J. Santamaria, Colossal ionic conductivity at interfaces of epitaxial ZrO₂:Y₂O₃ / SrTiO₃ heterostructures. *Science* **321**, 676–680 (2008).
12. N. Nakagawa, H. Y. Hwang, D. A. Muller, Why some interfaces cannot be sharp. *Nat. Mater.* **5**, 204–209 (2006).
13. M. Takizawa, H. Wadati, K. Tanaka, M. Hashimoto, T. Yoshida, A. Fujimori, A. Chikamatsu, H. Kumigashira, M. Oshima, K. Shibuya, T. Mihara, T. Ohnishi, M. Lippmaa, M. Kawasaki, H. Koinuma, S. Okamoto, A. J. Millis, Photoemission from buried interfaces in SrTiO₃/LaTiO₃ superlattices. *Phys. Rev. Lett.* **97**, 057601 (2006).
14. M. Basletic, J. L. Maurice, C. Carrétéro, G. Herranz, O. Copie, M. Bibes, E. Jacquet, K. Bouzehouane, S. Fusil, A. Barthélémy, Mapping the spatial distribution of charge carriers in LaAlO₃/SrTiO₃ heterostructures. *Nat. Mater.* **7**, 621–625 (2008).
15. Y. Chen, N. Pryds, J. E. Kleibeuker, G. Koster, J. Sun, E. Stamate, B. Shen, G. Rijnders, S. Linderoth, Metallic and insulating interfaces of amorphous SrTiO₃-based oxide heterostructures. *Nano Lett.* **11**, 3774–3778 (2011).
16. G. Herranz, M. Basletić, M. Bibes, C. Carrétéro, E. Tafra, E. Jacquet, K. Bouzehouane, C. Deranlot, A. Hamzić, J. M. Broto, A. Barthélémy, A. Fert, High mobility in LaAlO₃/SrTiO₃ heterostructures: Origin, dimensionality, and perspectives. *Phys. Rev. Lett.* **98**, 216803 (2007).
17. A. Kalabukhov, R. Gunnarsson, J. Börjesson, E. Olsson, T. Claeson, D. Winkler, Effect of oxygen vacancies in the SrTiO₃ substrate on the electrical properties of the LaAlO₃/SrTiO₃ interface. *Phys. Rev. B* **75**, 121404 (2007).
18. M. L. Scullin, J. Ravichandran, C. Yu, M. Huijben, J. Seidel, A. Majumdar, R. Ramesh, Pulsed laser deposition-induced reduction of SrTiO₃ crystals. *Acta Mater.* **58**, 457–463 (2010).
19. C. W. Schneider, M. Esposito, I. Marozau, K. Conder, M. Doebeli, Y. Hu, M. Mallepell, A. Wokaun, T. Lippert, The origin of oxygen in oxide thin films: Role of the substrate. *Appl. Phys. Lett.* **97**, 192107 (2010).
20. H. N. Lee, S. S. Ambrose Seo, W. S. Choi, C. M. Rouleau, Growth control of oxygen stoichiometry in homoepitaxial SrTiO₃ films by pulsed laser epitaxy in high vacuum. *Sci. Rep.* **6**, 19941 (2016).
21. F. V. E. Hensling, C. Xu, F. Gunkel, R. Dittmann, Unraveling the enhanced oxygen vacancy formation in complex oxides during annealing and growth. *Sci. Rep.* **7**, 39953 (2017).
22. D. Stender, S. Cook, J. A. Kilner, K. Döbeli, T. Lippert, A. Wokaun, SIMS of thin films grown by pulsed laser deposition on isotopically labeled substrates. *Solid State Ion.* **249–250**, 56–62 (2013).
23. J. D. Ferguson, Y. Kim, L. F. Kourkoutis, A. Vodnick, A. R. Woll, D. A. Muller, J. D. Brock, Epitaxial oxygen getter for a brownmillerite phase transformation in manganite films. *Adv. Mater.* **23**, 1226–1230 (2011).
24. Y.-M. Kim, J. He, M. D. Biegalski, H. Ambaye, V. Lauter, H. M. Christen, S. T. Pantelides, S. J. Pennycook, S. V. Kalinin, A. Y. Borisevich, Probing oxygen vacancy concentration and homogeneity in solid-oxide fuel-cell cathode materials on the subunit-cell level. *Nat. Mater.* **11**, 888–894 (2012).
25. D. A. Muller, N. Nakagawa, A. Ohtomo, J. L. Grazul, D. Hwang, Atomic-scale imaging of nanoengineered oxygen vacancy profiles in SrTiO₃. *Nature* **430**, 657–661 (2004).
26. C. Zhang, M. E. Grass, A. H. McDaniel, S. C. DeCaluwe, F. El Gabaly, Z. Liu, K. F. McCarty, R. L. Farrow, M. A. Linne, Z. Hussain, G. S. Jackson, H. Bluhm, B. W. Eichhorn, Measuring fundamental properties in operating solid oxide electrochemical cells by using in situ X-ray photoelectron spectroscopy. *Nat. Mater.* **9**, 944–949 (2010).
27. M. Nonnenmacher, M. P. O'Boyle, H. K. Wickramasinghe, Kelvin probe force microscopy. *Appl. Phys. Lett.* **58**, 2921 (1991).
28. K. V. Hansen, Y. Wu, T. Jacobsen, M. B. Mogensen, L. Theil Kuhn, Improved controlled atmosphere high temperature scanning probe microscope. *Rev. Sci. Instrum.* **84**, 073701 (2013).
29. S. S. Nonnenmann, A hot tip: Imaging phenomena using in situ multi-stimulus probes at high temperatures. *Nanoscale* **8**, 3164–3180 (2016).
30. S. S. Nonnenmann, R. Kungas, J. Vohs, D. A. Bonnell, Direct in situ probe of electrochemical processes in operating fuel cells. *ACS Nano* **7**, 6330–6336 (2013).
31. S. S. Nonnenmann, D. A. Bonnell, Miniature environmental chamber enabling in situ scanning probe microscopy within reactive environments. *Rev. Sci. Instrum.* **84**, 073707 (2013).
32. J. Zhu, C. R. Pérez, T.-S. Oh, R. Küngas, J. M. Vohs, D. A. Bonnell, S. S. Nonnenmann, Probing local electrochemical activity within yttria-stabilized-zirconia via in situ high-temperature atomic force microscopy. *J. Mater. Res.* **30**, 357–363 (2015).
33. J. Zhu, J. Wang, D. S. Mebane, S. S. Nonnenmann, In situ surface potential evolution along Au/Gd:CeO₂ electrode interfaces. *APL Mater.* **5**, 042503 (2017).
34. R. A. De Souza, Oxygen diffusion in SrTiO₃ and related perovskite oxides. *Adv. Funct. Mater.* **25**, 6326–6342 (2015).
35. R. Meyer, A. F. Zurhelle, R. A. De Souza, R. Waser, F. Gunkel, Dynamics of the metal-insulator transition of donor-doped SrTiO₃. *Phys. Rev. B* **94**, 115408 (2016).
36. K. Gömann, G. Borchardt, M. Schulz, A. Gömann, W. Maus-Friedrichs, B. Lesage, O. Kaïtasov, S. Hoffmann-Eifert, T. Schneller, Sr diffusion in undoped and La-doped SrTiO₃ single crystals under oxidizing conditions. *Phys. Chem. Chem. Phys.* **7**, 2053–2060 (2005).
37. R. Meyer, R. Waser, J. Helmbold, G. Borchardt, Observation of vacancy defect migration in the cation sublattice of complex oxides by ¹⁸O tracer experiments. *Phys. Rev. Lett.* **90**, 105901 (2003).
38. R. Waser, Bulk conductivity and defect chemistry of acceptor-doped strontium titanate in the quenched state. *J. Am. Ceram. Soc.* **74**, 1934–1940 (1991).
39. S. V. Kalinin, D. A. Bonnell, Screening phenomena on oxide surfaces and its implications for local electrostatic and transport measurements. *Nano Lett.* **4**, 555–560 (2004).
40. E. Koren, Y. Rosenwaks, J. E. Allen, E. R. Hemesath, L. J. Lauhon, Nonuniform doping distribution along silicon nanowires measured by Kelvin probe force microscopy and scanning photocurrent microscopy. *Appl. Phys. Lett.* **95**, 092105 (2009).
41. Q. Chen, L. Mao, Y. Li, T. Kong, N. Wu, C. Ma, S. Bai, Y. Jin, D. Wu, W. Lu, B. Wang, L. Chen, Quantitative operando visualization of the energy band depth profile in solar cells. *Nat. Commun.* **6**, 7745 (2015).
42. F. V. E. Hensling, D. J. Keeble, J. Zhu, S. Brose, C. Xu, F. Gunkel, S. Danyluk, S. S. Nonnenmann, W. Egger, R. Dittmann, UV radiation enhanced oxygen vacancy formation caused by the PLD plasma plume. *Sci. Rep.* **8**, 8846 (2018).
43. C. Maragliano, S. Lilliu, M. S. Dahlem, M. Chiesa, T. Souier, M. Stefancich, Quantifying charge carrier concentration in ZnO thin films by scanning Kelvin probe microscopy. *Sci. Rep.* **4**, 4203 (2014).
44. S. Das, B. Wang, Y. Cao, M. R. Cho, Y. J. Shin, S. M. Yang, L. Wang, M. Kim, S. V. Kalinin, L.-Q. Chen, T. W. Noh, Controlled manipulation of oxygen vacancies using nanoscale flexoelectricity. *Nat. Commun.* **8**, 615 (2017).
45. Y. Kozuka, Y. Hikita, C. Bell, H. Y. Hwang, Dramatic mobility enhancements in doped SrTiO₃ thin films by defect management. *Appl. Phys. Lett.* **97**, 012107 (2010).
46. R. A. De Souza, A. H. H. Ramadan, Ionic conduction in the SrTiO₃|YSZ|SrTiO₃ heterostructure. *Phys. Chem. Chem. Phys.* **15**, 4505–4509 (2013).
47. J. Maier, *Physical Chemistry of Ionic Materials: Ions and Electrons in Solids* (John Wiley & Sons, 2004).
48. R. A. De Souza, V. Metlenko, D. Park, T. E. Weirich, Behavior of oxygen vacancies in single-crystal SrTiO₃: Equilibrium distribution and diffusion kinetics. *Phys. Rev. B* **85**, 174109 (2012).
49. R. A. De Souza, Limits to the rate of oxygen transport in mixed-conducting oxides. *J. Mater. Chem. A* **5**, 20334–20350 (2017).

50. R. Waser, M. Aono, Nanoionics-based resistive switching memories. *Nat. Mater.* **6**, 833–840 (2007).

51. S. Ohta, T. Nomura, H. Ohta, K. Koumoto, High-temperature carrier transport and thermoelectric properties of heavily La- or Nb-doped SrTiO$_3$ single crystals. *J. Appl. Phys.* **97**, 034106 (2005).

52. R. Kim, M. Lundstrom, "Notes on Fermi-Dirac integrals (3rd edition)" (2008); https://nanohub.org/resources/5475.

53. E. Mikheev, B. D. Hoskins, D. B. Strukov, S. Stemmer, Resistive switching and its suppression in Pt/Nb:SrTiO$_3$ junctions. *Nat. Commun.* **5**, 3990 (2014).

54. B. Nagaraj, T. Wu, S. B. Ogale, T. Venkatesan, R. Ramesh, Interface characterization of all-perovskite oxide field effect heterostructures. *J. Electroceram.* **8**, 233–241 (2002).

Science Advances

Probing vacancy behavior across complex oxide heterointerfaces

Jiaxin Zhu, Jung-Woo Lee, Hyungwoo Lee, Lin Xie, Xiaoqing Pan, Roger A. De Souza, Chang-Beom Eom and Stephen S. Nonnenmann

ARTICLE TOOLS	http://advances.sciencemag.org/content/5/2/eaau8467
SUPPLEMENTARY MATERIALS	http://advances.sciencemag.org/content/suppl/2019/02/15/5.2.eaau8467.DC1
REFERENCES	This article cites 52 articles, 4 of which you can access for free http://advances.sciencemag.org/content/5/2/eaau8467#BIBL
PERMISSIONS	http://www.sciencemag.org/help/reprints-and-permissions

Use of this article is subject to the Terms of Service